



## Interocular symmetry of foveal cone topography in congenital achromatopsia

Katie M. Litts, Michalis Georgiou, Christopher S. Langlo, Emily J. Patterson, Rebecca R. Mastey, Angelos Kalitzeos, Rachel E. Linderman, Byron L. Lam, Gerald A. Fishman, Mark E. Pennesi, Christine N. Kay, William W. Hauswirth, Michel Michaelides & Joseph Carroll

To cite this article: Katie M. Litts, Michalis Georgiou, Christopher S. Langlo, Emily J. Patterson, Rebecca R. Mastey, Angelos Kalitzeos, Rachel E. Linderman, Byron L. Lam, Gerald A. Fishman, Mark E. Pennesi, Christine N. Kay, William W. Hauswirth, Michel Michaelides & Joseph Carroll (2020): Interocular symmetry of foveal cone topography in congenital achromatopsia, Current Eye Research, DOI: [10.1080/02713683.2020.1737138](https://doi.org/10.1080/02713683.2020.1737138)

To link to this article: <https://doi.org/10.1080/02713683.2020.1737138>



Accepted author version posted online: 28 Feb 2020.



Submit your article to this journal [↗](#)



Article views: 5



View related articles [↗](#)



View Crossmark data [↗](#)

**Publisher:** Taylor & Francis

**Journal:** *Current Eye Research*

**DOI:** 10.1080/02713683.2020.1737138

*For Current Eye Research*

**Interocular symmetry of foveal cone topography in congenital achromatopsia**

Katie M. Litts<sup>1</sup>, Michalis Georgiou<sup>2,3</sup>, Christopher S. Langlo<sup>4</sup>, Emily J. Patterson<sup>1</sup>, Rebecca R. Mastey<sup>1</sup>, Angelos Kalitzeos<sup>2,3</sup>, Rachel E. Linderman<sup>4</sup>, Byron L. Lam<sup>5</sup>, Gerald A. Fishman<sup>6</sup>, Mark E. Pennesi<sup>7</sup>, Christine N. Kay<sup>8</sup>, William W. Hauswirth<sup>9</sup>, Michel Michaelides<sup>2,3</sup>, Joseph Carroll<sup>1,4</sup>

1. Ophthalmology & Visual Sciences, Medical College of Wisconsin, Milwaukee, Wisconsin, United States of America
2. Moorfields Eye Hospital, London, United Kingdom
3. UCL Institute of Ophthalmology, University College London, London, United Kingdom
4. Cell Biology, Neurobiology and Anatomy, Medical College of Wisconsin, Milwaukee, Wisconsin, United States of America
5. Bascom Palmer Eye Institute, University of Miami, Miami, Florida, United States of America
6. Pangere Center for Inherited Retinal Diseases, The Chicago Lighthouse, Chicago, Illinois, United States
7. Casey Eye Institute, Oregon Health & Science University, Portland, OR 97239
8. Vitreoretinal Associates, Gainesville, Florida, United States
9. Ophthalmology, University of Florida, Gainesville, Florida, United States

Corresponding author: Joseph Carroll, Department of Ophthalmology & Visual Sciences,

Medical College of Wisconsin, 925 N 87th St, Milwaukee, WI 53226-0509

Email: jcarroll@mcw.edu; Phone: (414) 955-2052

Manuscript word count: 2691

Funding: Research reported in this publication was supported by the National Eye Institute of the National Institutes of Health under award numbers R01EY017607, P30EY001931, P30EY010572, R24EY022023, T32EY014537, T32GM080202, and F32EY029148, by the National Center for Advancing Translational Sciences under award number UL1TR001436, unrestricted grant from Research to Prevent Blindness to CEI, the National Institute for Health Research Biomedical Research Centre at Moorfields Eye Hospital NHS Foundation Trust and

UCL Institute of Ophthalmology, Onassis Foundation, Leventis Foundation, The Wellcome Trust (099173/Z/12/Z), Moorfields Eye Hospital Special Trustees, Moorfields Eye Charity, Retina UK, and the Foundation Fighting Blindness (USA). This investigation was conducted in part in a facility constructed with support from a Research Facilities Improvement Program, grant number C06RR016511 from the National Center for Research Resources, NIH. The content is solely the responsibility of the authors and does not necessarily represent the official views of the National Institutes of Health. Additional support was provided by the Gene and Ruth Posner Foundation (Milwaukee, WI) and Applied Genetics Technology Corporation (Alachua, FL).

Disclosures: Joseph Carroll has received funding support from Applied Genetic Technologies Corporation, consultant fees from MeiraGTx, and personal financial interest in Translational Imaging Innovations. Michel Michaelides has received consultant fees from MeiraGTx. Mark Pennesi and Byron Lam have received funding support from Applied Genetic Technologies Corporation. Christine Kay has received funding support and consultant fees from Applied Genetic Technologies Corporation. The authors report no other conflicts of interest. The authors alone are responsible for the content and writing of the paper.

Accepted Manuscript

## Abstract

**Purpose:** To determine interocular symmetry of foveal cone topography in achromatopsia (ACHM) using non-confocal split-detection adaptive optics scanning light ophthalmoscopy (AOSLO).

**Methods:** Split-detector AOSLO images of the foveal cone mosaic were acquired from both eyes of 26 subjects (mean age 24.3 years; range 8 – 44 years, 14 females) with genetically confirmed *CNGA3*- or *CNGB3*-associated ACHM. Cones were identified within a manually delineated rod-free zone. Peak cone density (PCD) was determined using an  $80 \times 80 \mu\text{m}$  sampling window within the rod-free zone. The mean and standard deviation (SD) of intercell distance (ICD) were calculated to derive the coefficient of variation (CV). Cone density difference maps were generated to compare cone topography between eyes.

**Results:** PCD (mean  $\pm$  SD) was  $17,530 \pm 9,614$  cones/ $\text{mm}^2$  and  $17,638 \pm 9,753$  cones/ $\text{mm}^2$  for right and left eyes, respectively ( $p = 0.677$ , Wilcoxon test). The mean ( $\pm$  SD) for ICD was  $9.05 \pm 2.55 \mu\text{m}$  and  $9.24 \pm 2.55 \mu\text{m}$  for right and left eyes, respectively ( $p = 0.410$ , paired t test). The mean ( $\pm$  SD) for CV of ICD was  $0.16 \pm 0.03$  and  $0.16 \pm 0.04$  for right and left eyes, respectively ( $p = 0.562$ , paired t test). Cone density maps demonstrated that cone topography of the ACHM fovea is non-uniform with local variations in cone density between eyes.

**Conclusions:** These results demonstrate interocular symmetry of the foveal cone mosaic (both density and packing) in ACHM. As cone topography can differ between eyes of a subject, PCD does not completely describe the foveal cone mosaic in ACHM. Nonetheless, these findings are of value in longitudinal monitoring of patients during treatment trials and further suggest that both eyes of a given subject may have similar therapeutic potential and non-study eye can be used as a control.

**Keywords:** achromatopsia, interocular symmetry, fovea, retinal imaging, cone photoreceptors

## Introduction

Congenital achromatopsia (ACHM) is a retinal disease associated with substantially reduced or absent cone function, severely impaired or absent color vision, nystagmus, photoaversion, and reduced visual acuity.<sup>1</sup> While ACHM has been linked to disease-causing sequence variants in *CNGA3*, *CNGB3*, *GNAT2*, *PDE6C*, *PDE6H*, and *ATF6* genes,<sup>2-6</sup> approximately 70% of ACHM cases are associated with variants in the subunits of the cyclic nucleotide-gated ion channel (*CNGA3* and *CNGB3*).<sup>7</sup> Despite severely impaired cone function, recent studies utilizing adaptive optics scanning light ophthalmoscopy (AOSLO) and optical coherence tomography (OCT) have demonstrated the presence of remnant foveal cone structure in most patients with ACHM.<sup>8-11</sup> These remnant cones serve as the cellular target for gene therapy trials for ACHM, and thus there is great interest in understanding the variability in cone structure across patients.

Besides inter-subject variation, there is interest in characterizing differences in foveal structure within a subject. For example, assessing the interocular symmetry of foveal cone structure may be important for selection of patients and monitoring outcomes in clinical trials, where the contralateral eye could be used as a control. Interocular symmetry of foveal outer nuclear layer (ONL) thickness<sup>11</sup> and the integrity of the ellipsoid zone<sup>8,12</sup> have been recently demonstrated in patients with ACHM. However, as the appearance of the ellipsoid zone and the ONL thickness do not necessarily correlate with the degree of remnant cone structure on AOSLO,<sup>8</sup> it cannot be assumed that this symmetry extends to the foveal cone mosaic. Therefore, the purpose of this study is to assess interocular cellular symmetry through detailed examination of the topography of the foveal cone mosaic in ACHM using non-confocal split-detector AOSLO.

## Methods

### Subjects

This research followed the tenets of the Declaration of Helsinki and was approved by the

Institutional Review Boards at the Medical College of Wisconsin (PRO00030741) and Moorfields Eye Hospital. Written informed consent was obtained from all participants and their information stored in a database (Lattice Version 1.0, Translational Imaging Innovations, Inc., Hickory, NC). Images from 26 patients (mean age 24.3 years; range 8 – 44 years; 14 females) with genetically confirmed *CNGA3*- or *CNGB3*-associated ACHM (2 and 24 subjects, respectively) were used for this study. Twenty-one subjects were recruited as part of other studies and have appeared in previous publications (**Table 1**).<sup>8-17</sup> Best corrected visual acuity (BCVA) was measured for each eye using either the Early Treatment Diabetic Retinopathy Study chart or the Electronic Visual Acuity protocol.

#### AOSLO imaging

Prior to imaging, subjects had their pupils dilated with one drop each of 1% tropicamide and 2.5% phenylephrine or one drop of Cyclomydril only. Both eyes of each subject were imaged using a custom-built AOSLO, housed at either Medical College of Wisconsin or Moorfields Eye Hospital, as previously described.<sup>18,19</sup> In brief, a 790 nm light source was used for imaging and an 850 nm light source was used for wavefront sensing. The power of these light sources measured at the cornea was 70 and 17  $\mu$ W, respectively.<sup>14</sup> The head of each subject was stabilized by a dental impression on a bite bar. Simultaneous confocal and non-confocal split-detector AOSLO images focused on the foveal cone mosaic were acquired in absolute spatial and temporal co-registration, as previously described.<sup>8</sup> The imaging protocol included a 5° square grid centered on the fovea, sampled at 1° intervals using 1° to 1.75° square fields of view. Image sequences consisting of 150 to 200 frames with an acquisition rate of 16.6 frames/second were recorded at different locations using a fixation target.

The raw frames from each image sequence were corrected for sinusoidal distortions and strip-registered to a reference frame, as previously described.<sup>20,21</sup> For each eye, the confocal and

split-detector AOSLO images were montaged simultaneously either manually or semi-automatically using a multi-modal montaging algorithm<sup>22</sup> and Adobe Photoshop CS6 (Adobe Systems, Inc., San Jose, CA, USA). The linear scale of the AOSLO images for a given subject ( $S'_{R(x)}$ ; units:  $\mu\text{m}/\text{pixel}$ ) was estimated by using the following equation:

$$S'_{R(x)} = \frac{T}{f_l T_s} \left( \frac{180}{\pi} \right) RMF \left( \frac{l_A}{l_{A,0}} \right)$$

Where  $T$  represents the periodicity of a Ronchi ruling ( $\mu\text{m}/\text{cycles}$ ),  $f_l$  represents the focal length of the model eye in our system ( $\mu\text{m}$ ),  $T_s$  represents the sampling period between lines in the Ronchi ruling (pixels/cycle),  $RMF$  represents the assumed retinal magnification factor (291  $\mu\text{m}/\text{degree}$ ) of an eye with a 24.0 mm axial length (represented by  $l_{A,0}$ ),<sup>23</sup> and  $l_A$  represents the actual axial length of the subject's eye in mm (measured with an IOL Master, Carl Zeiss Meditec, Inc., Dublin, CA).

#### Analysis of cone metrics

Using a previously published method,<sup>8</sup> the approximate extent of the rod-free zone at the fovea was defined for each eye. The area of the rod-free zone was measured by outlining the region with the polygon tool and using the scale of the AOSLO montage in ImageJ.<sup>24</sup> All cones within the delineated rod-free zone were manually and semi-automatically<sup>25</sup> identified and represented by their coordinate location within the split-detector image. For this study, an  $80 \times 80 \mu\text{m}$  sample window was then used to determine density in cones per square millimeter at each pixel within the coordinate array using custom Matlab software (Mathworks Inc., Natick, MA USA). All cone coordinates within the sample window were included in the measurement. Cone density maps were generated using the cone coordinates across the rod-free zone, and the location of maximum cone density (i.e., peak cone density, PCD) was used to anchor subsequent

analyses. As there were often multiple pixel locations with the same cone density value, the cone density at the location centered between these locations was used as the PCD.

Cone packing metrics (inter cell distance [ICD] and coefficient of variation [CV] of ICD) were determined using all identified cone coordinates within an  $80 \times 80 \mu\text{m}$  region centered on the location of PCD for each fovea. ICD was calculated as the average distance between a cell and all of its immediate neighbors for all cells within a region of interest, and CV of ICD was calculated as the standard deviation of ICD divided by the mean ICD.<sup>8</sup>

To compare overall cone topography between eyes of a subject, a difference map was generated by calculating the absolute value of the difference in cone density at each overlapping pixel within the rod-free zones of each eye. Density maps for left eyes were flipped to be in the same nasal-temporal orientation as right eyes. The density maps were then aligned using their respective PCD location. Before subtracting the density maps, the map with the larger scale ( $\mu\text{m}/\text{pixel}$ ) was resampled using nearest-neighbor interpolation to match the scale of the map from the other eye. Because the size and shape of the rod-free zone as well as the location of the PCD within the rod-free zone differed between the two eyes of a give subject, the size of the resultant density map was always smaller than the density map for either individual eye for that subject.

### Statistical analysis

Statistical analyses were completed using Prism 8 (GraphPad, La Jolla, CA, USA). Raw values and interocular differences for each metric were tested for normality using the Shapiro-Wilk test (with  $p < 0.05$  as criterion) to guide use of statistical methods as appropriate. Linear regressions were plotted to determine correlations between eyes. Raw PCD values and BCVA between eyes did not pass normality testing; therefore, the Wilcoxon signed-rank test was used to test for

significant differences between eyes. For cone packing metrics (ICD and CV of ICD), raw values and interocular differences passed normality testing and a paired t test was used to test for differences between eyes. Bland-Altman analysis for each metric was used to examine the limits of interocular agreement.<sup>26,27</sup>

## Results

For BCVA, the mean  $\pm$  standard deviation (SD) was  $0.87 \pm 0.20$  logMAR for right eyes and  $0.87 \pm 0.21$  logMAR for left eyes. The BCVA was not significantly different between eyes (Wilcoxon signed rank test,  $p = 0.714$ ). BCVA for each subject is listed in **Table 1**.

Cone metrics were analyzed within the rod-free zone, which had an area (mean  $\pm$  SD) of  $0.16 \pm 0.09$  mm<sup>2</sup> and  $0.17 \pm 0.11$  mm<sup>2</sup> for right and left eyes, respectively. For PCD, the mean  $\pm$  SD was  $17,530 \pm 9,614$  cones/mm<sup>2</sup> for right eyes and  $17,638 \pm 9,753$  cones/mm<sup>2</sup> for left eyes. Across subjects, the PCD was not significantly different between eyes (Wilcoxon signed rank test,  $p = 0.677$ ). Linear regression analysis showed a strong correlation between eyes (**Figure 1A**). Bland-Altman analysis of the PCD showed good agreement between eyes, with a mean bias (OD – OS) of  $-108$  cones/mm<sup>2</sup> (CI  $-1093$  cones/mm<sup>2</sup> to  $877$  cones/mm<sup>2</sup>), and 95% of the differences falling between  $-5132$  cones/mm<sup>2</sup> and  $4916$  cones/mm<sup>2</sup> (**Figure 1D**). An example of a subject with good symmetry by PCD (determined by a small percent difference, 6%) is shown in **Figure 2A-B**. An example of a subject with the worst symmetry by PCD (determined by the largest percent difference, 56%) is shown in **Figure 2C-D**.

For ICD, the mean  $\pm$  SD was  $9.05 \pm 2.55$   $\mu$ m and  $9.24 \pm 2.55$   $\mu$ m for right and left eyes, respectively. The ICD was not significantly different between eyes (paired t test,  $p = 0.410$ ,  $t = 0.8384$ ,  $df = 25$ ). Linear regression analysis showed a strong correlation between eyes (**Figure 1B**). Bland-Altman analysis showed good agreement between eyes, with a mean bias (OD –

OS) for ICD of  $-0.19 \mu\text{m}$  (CI  $-0.63 \mu\text{m}$  to  $0.25 \mu\text{m}$ ), and 95% of the differences falling between  $-2.45 \mu\text{m}$  and  $2.07 \mu\text{m}$  (**Figure 1E**). An example of a subject with good symmetry by ICD (6.5% difference) is shown in **Figure 3A-B**. An example of a subject with the worst symmetry by ICD (30% difference) is shown in **Figure 3C-D**.

For CV of ICD, the mean  $\pm$  SD was  $0.16 \pm 0.03 \mu\text{m}$  and  $0.16 \pm 0.04 \mu\text{m}$  for right and left eyes, respectively. Although the CV of ICD was not significantly different between eyes (paired t test,  $p = 0.562$ ,  $t = 0.5880$ ,  $df = 25$ ), linear regression showed a weak correlation (**Figure 1C**). Bland-Altman analysis showed good agreement between eyes with a mean bias (OD – OS) for CV of ICD of  $0.003$  (CI  $-0.01$  to  $0.02$ ), and 95% of the differences falling between  $-0.06$  and  $0.07$  (**Figure 1F**). The subject in **Figure 3C-D** had the best symmetry by CV of ICD (1% difference). An example of a subject with good symmetry by CV of ICD (CV of ICD interocular difference of  $-0.01$ ) is shown in **Figure 4A-B**. An example of a subject with the second-worst symmetry by CV of ICD (46% difference) is shown in **Figure 4C-D**.

As PCD gives information about the maximum density at only one location in a given fovea, we also examined the topography of cone density across the rod-free zone in ACHM (**Figure 5**). Cone density across the ACHM fovea is non-uniform. A subject with good interocular symmetry by PCD (JC\_10216) also demonstrates similar interocular cone topography with local areas of divergent cone density. In contrast, the subject with the worst interocular symmetry by PCD (JC\_10232) demonstrates dissimilar interocular cone topography. In addition, some eyes contained multiple areas of high density, as in JC\_0047, with local variation in cone density surrounding the PCD location and secondary areas of high density.

## Discussion

Here we demonstrate interocular symmetry of the remnant foveal cone mosaic in patients with ACHM. In addition to this symmetry, the remaining cone density is significantly lower than that seen in individuals with normal vision.<sup>28-30</sup> The Bland-Altman analysis indicates that interocular differences for PCD are expected to be less than 4928 cones/mm<sup>2</sup> (28%) for 95% of subjects with ACHM. While other metrics of cone packing (ICD and CV of ICD) also showed no significant differences between eyes, there was more variability in these metrics. There was also a high degree of variability in the qualitative topography of the cone mosaic within the rod-free zone, suggesting that PCD should not necessarily be used as a single descriptor to represent the degree of remnant cone structure in patients with ACHM. Nonetheless, our data are in agreement with recent work from Georgiou et al.,<sup>10</sup> who observed no significant difference in PCD, ICD, or CV of ICD in seven subjects with *CNGA3*-associated ACHM.

Collectively, these data are similar to observations made in patients with ACHM using other imaging modalities. For example, Sundaram et al.<sup>12</sup> and Langlo et al.<sup>8</sup> reported symmetry in the grade of the ellipsoid zone disruption on OCT (using this fact to support a study design in which they conducted more detailed analyses in just one eye of each subject). In addition, Matet et al.<sup>31</sup> found no interocular difference in the size of ellipsoid zone defect on OCT. Mastey et al.<sup>11</sup> also demonstrated no significant difference in foveal ONL thickness in 76 subjects with ACHM (though the ONL thickness was generally reduced compared to control subjects). In addition, Matet et al.<sup>31</sup> showed no difference between eyes in the extent of the hyperautofluorescent perifoveal ring observed using short-wavelength autofluorescence or the extent of the central hypofluorescence observed using near-infrared autofluorescence. Aboshiha et al.<sup>17</sup> also reported no difference in fundus autofluorescence between eyes in a cohort of 38 patients with ACHM. The lack of interocular differences in patients with ACHM, and the fact that symmetry is also observed in subjects with normal vision for both PCD<sup>32</sup> and foveal ONL thickness<sup>11</sup> is consistent with a symmetrical disease process in ACHM.

In addition to structural symmetry, there is functional symmetry (e.g., visual acuity, contrast sensitivity, and microperimetry) in patients with ACHM. Consistent with our result in a population of mostly patients with *CNGB3*-associated ACHM, no significant interocular difference in BCVA in patients with *CNGA3*-associated ACHM has been reported.<sup>10,33</sup> Matet et al.<sup>31</sup> also showed a strong correlation between visual acuity from right and left eyes in patients with ACHM ( $r = 0.82$ ,  $p = 0.001$ ). In addition, Zobor et al.<sup>33</sup> demonstrated a lack of significant interocular difference in functional results, including contrast sensitivity and microperimetry in patients with ACHM and Aboshiha et al.<sup>34</sup> found no significant interocular difference in dark adaptation thresholds in patients with ACHM. Together with our findings of structural symmetry in AOSLO, these data suggest that both eyes of a given subject may have similar therapeutic potential.

Our study has a number of limitations. First, we only assessed the foveal cone mosaic. As the foveal cone mosaic drives the majority of our normal visual function, a logical focus has been on using the degree of remnant foveal cone structure to estimate the therapeutic potential for improving vision in ACHM.<sup>8</sup> However, it is not clear to what extent restoring parafoveal cone function would improve the non-acuity-related symptoms of ACHM (e.g., nystagmus, photoaversion). There has been minimal assessment of parafoveal cone structure in ACHM,<sup>15</sup> and thus the intraocular topography and interocular symmetry of parafoveal cone structure is not known. Second, the foveal cone analyses relied on cone identification by a single observer. It has been shown that cone identification in AOSLO images from patients with ACHM can show differences across observers of varying expertise.<sup>13</sup> While we do not think this affects the conclusion of interocular symmetry using a single experienced observer, deriving accurate estimates of remnant cone structure in ACHM may benefit from the use of multiple observers or automated cone identification algorithms.<sup>25,35-37</sup> Additionally, as we only included subjects with quantifiable AOSLO images in both eyes, it is possible that this may have introduced some bias.

Finally, as the “rod-free zone” was subjectively identified and is not a clear boundary, we cannot exclude the presence of rod structure within this area. The area of this rod-free zone in the ACHM fovea was smaller than that previously reported by histology in the normal fovea, which is estimated to be about 0.3 mm<sup>2</sup> (horizontal diameter = 0.35 mm; axial ratio = 1.29) with rods appearing 100 to 200 μm from the center of the fovea.<sup>38</sup> We did not assess the rod mosaic, but the degree to which rod structure encroaches on the foveal center may influence the topography of the cone mosaic and could also underlie downstream visual disruptions in the visual system, such as the rod-driven activity reported in the foveal representation of the primary visual cortex.<sup>39</sup> Fully classifying therapeutic potential in patients with ACHM will require additional comprehensive analyses of the photoreceptor mosaic in future studies.

### **Acknowledgements**

The authors would like to thank Alexander Salmon, Erica Woertz, and Jenna Cava for helpful discussions, Phyllis Summerfelt for facilitating subject visits, Brian Higgins for managing data, and Erin Curran for managing human subject protocols.

Presented in part at ARVO Annual Meeting 2018 in Honolulu, HI and FASEB Biology and Chemistry of Vision Conference 2019, in Steamboat Springs, CO.

## Figure Captions

**Figure 1.** Foveal cone metrics demonstrate interocular symmetry in ACHM. Shown are linear regression (A-C) and Bland-Altman plots (D-F) for peak cone density, inter cell distance (ICD), and coefficient of variation (CV) of ICD, respectively. For the linear regression analysis, each open circle represents data from the right and left eyes of a given subject, the solid line represents linear regression for right and left eye data, and the dashed lines represent the 95% confidence interval for each regression. For the Bland-Altman plots, the solid line represents average bias between the eyes, dashed lines represent limits of agreement, and gray shading represents confidence intervals for the bias and limits of agreement.

**Figure 2.** Examples of interocular symmetry in ACHM by peak cone density (PCD). Shown are split-detector AOSLO images of the fovea in two subjects with ACHM. JC\_10216 had good interocular symmetry by PCD (6% difference), with 12,031 cones/mm<sup>2</sup> in the right eye (A) and 12,813 cones/mm<sup>2</sup> in the left eye (B). JC\_10232 had the worst interocular symmetry by PCD (56% difference), with 9,688 cones/mm<sup>2</sup> in the right eye (C) and 5,469 cones/mm<sup>2</sup> in the left eye (D). White cross, location of PCD. Scale bar, 100  $\mu$ m.

**Figure 3.** Examples of interocular symmetry in ACHM by inter cell distance (ICD). Shown are split-detector AOSLO images of the fovea in two subjects with ACHM. JC\_10024 had good interocular symmetry by ICD (6.5% difference) with 5.87  $\mu$ m in the right eye (A) and 6.27  $\mu$ m in the left eye (B). JC\_0047 had the worst interocular symmetry by ICD (30% difference) with 8.63  $\mu$ m in the right eye (C) and 11.62  $\mu$ m in the left eye (D). Images were minimally adjusted for brightness and contrast for display only. White cross, location of peak cone density. Scale bar, 100  $\mu$ m.

**Figure 4.** Examples of interocular symmetry in ACHM by coefficient of variation of inter cell distance (CV of ICD). Shown are split-detector AOSLO images of the fovea in two subjects with ACHM. JC\_10999 had good interocular symmetry by CV of ICD (12% difference), with 0.11 in the right eye (A) and 0.13 in the left eye (B). JC\_10195 had the second-worst interocular symmetry by CV of ICD (46% difference), with 0.22 in the right eye (C) and 0.14 in the left eye (D). Images were minimally adjusted for brightness and contrast for display only. White cross, location of peak cone density. Scale bar, 100  $\mu\text{m}$ .

**Figure 5.** Foveal cone photoreceptor topography in ACHM. Density maps showing cone density at every pixel within the rod-free zone in the right and left eyes of three subjects (OD and OS, first and second columns respectively). Data from the left eye is flipped to match the same nasal-temporal orientation as the right eye. Difference maps (third column) show absolute difference between right and left eyes of a subject. JC\_10216 is an example of good interocular symmetry by peak cone density (PCD) and JC\_10232 had the worst interocular symmetry by PCD as shown in figure 2. JC\_0047 shows an example of multiple areas of relatively high cone density within the rod-free zone. White cross, location of PCD. Scale bar, 100  $\mu\text{m}$ .

## References

1. Hirji N, Aboshiha J, Georgiou M, Bainbridge J, Michaelides M. Achromatopsia: Clinical features, molecular genetics, animal models and therapeutic options. *Ophthalmic Genet.* 2018;39(2):149-157.
2. Kohl S, Marx T, Giddings I, Jägle H, Jacobson SG, Apfelstedt-Sylla E, Zrenner E, Sharpe LT, Wissinger B. Total colourblindness is caused by mutations in the gene encoding the alpha-subunit of the cone photoreceptor cGMP-gated cation channel. *Nat Genet.* 1998;19(3):257-259.
3. Kohl S, Zobor D, Chiang W, Weisschuh N, Staller J, Menendez IG, Chang S, Beck SC, Garrido MG, Sothilingam V et al. Mutations in the unfolded protein response regulator *ATF6* cause the cone dysfunction disorder achromatopsia. *Nat Genet.* 2015;47(7):757-765.
4. Kohl S, Coppieters F, Meire F, Schaich S, Roosing S, Brennenstuhl C, Bolz S, van Genderen MM, Riemsdijk FC, European Retinal Disease Consortium et al. A nonsense mutation in *PDE6H* causes autosomal-recessive incomplete achromatopsia. *Am J Hum Genet.* 2012;91(3):527-532.
5. Kohl S, Baumann B, Brogghammer M, Jägle H, Sieving P, Kellner U, Spegal R, Anastasi M, Zrenner E, Sharpe LT et al. Mutations in the *CNGB3* gene encoding the beta-subunit of the cone photoreceptor cGMP-gated channel are responsible for achromatopsia (ACHM3) linked to chromosome 8q21. *Hum Mol Genet.* 2000;9(14):2107-2116.
6. Kohl S, Baumann B, Rosenberg T, Kellner U, Lorenz B, Vadalà M, Jacobson SG, Wissinger B. Mutations in the cone photoreceptor G-protein  $\alpha$ -subunit gene *GNAT2* in patients with achromatopsia. *Am J Hum Genet.* 2002;71(2):422-425.
7. Thiadens AA, Slingerland NW, Roosing S, van Schooneveld MJ, van Lith-Verhoeven JJ, van Moll-Ramirez N, van den Born LI, Hoyng CB, Cremers FP, Klaver CC. Genetic etiology

- and clinical consequences of complete and incomplete achromatopsia. *Ophthalmology*. 2009;116(10):1984-1989.
8. Langlo CS, Patterson EJ, Higgins BP, Summerfelt P, Razeen MM, Erker LR, Parker M, Collison FT, Fishman GA, Kay CN et al. Residual foveal cone structure in *CNGB3*-associated achromatopsia. *Invest Ophthalmol Vis Sci*. 2016;57(10):3984-3995.
  9. Langlo CS, Erker LR, Parker M, Patterson EJ, Higgins BP, Summerfelt P, Razeen MM, Collison FT, Fishman GA, Kay CN et al. Repeatability and longitudinal assessment of foveal cone structure in *CNGB3*-associated achromatopsia. *Retina*. 2017;37(10):1956-1966.
  10. Georgiou M, Litts KM, Kalitzeos A, Langlo CS, Kane T, Singh N, Kassilian M, Hirji N, Kumaran N, Dubra A et al. Adaptive optics retinal imaging in *CNGA3*-associated achromatopsia: Retinal characterization, interocular symmetry, and intrafamilial variability. *Invest Ophthalmol Vis Sci*. 2019;60(1):383-396.
  11. Mastey RR, Gaffney M, Litts KM, Langlo CS, Patterson EJ, Strampe MR, Kalitzeos A, Michaelides M, Carroll J. Assessing the interocular symmetry of foveal outer nuclear layer thickness in achromatopsia. *Transl Vis Sci Technol*. 2019;8(5):21.
  12. Sundaram V, Wilde C, Aboshiha J, Cowing J, Han C, Langlo CS, Chana R, Davidson AE, Sergouniotis PI, Bainbridge JW et al. Retinal structure and function in achromatopsia: implications for gene therapy. *Ophthalmology*. 2014;121(1):234-245.
  13. Abozaid MA, Langlo CS, Dubis AM, Michaelides M, Tarima S, Carroll J. Reliability and repeatability of cone density measurements in patients with congenital achromatopsia. *Adv Exp Med Biol*. 2016;854:277-283.
  14. Scoles D, Sulai YN, Langlo CS, Fishman GA, Curcio CA, Carroll J, Dubra A. In vivo imaging of human cone photoreceptor inner segments. *Invest Ophthalmol Vis Sci*. 2014;55(7):4244-4251.

15. Dubis AM, Cooper RF, Aboshiha J, Langlo CS, Sundaram V, Liu B, Collison F, Fishman GA, Moore AT, Webster AR et al. Genotype-dependent variability in residual cone structure in achromatopsia: towards developing metrics for assessing cone health. *Invest Ophthalmol Vis Sci.* 2014;55(11):7303-7311.
16. Hirji N, Georgiou M, Kalitzeos A, Bainbridge JW, Kumaran N, Aboshiha J, Carroll J, Michaelides M. Longitudinal assessment of retinal structure in achromatopsia patients with long-term follow-up. *Invest Ophthalmol Vis Sci.* 2018;59(15):5735-5744.
17. Aboshiha J, Dubis AM, Cowing J, Fahy RT, Sundaram V, Bainbridge JW, Ali RR, Dubra A, Nardini M, Webster AR et al. A prospective longitudinal study of retinal structure and function in achromatopsia. *Invest Ophthalmol Vis Sci.* 2014;55(9):5733-5743.
18. Dubra A, Sulai Y. Reflective afocal broadband adaptive optics scanning ophthalmoscope. *Biomed Opt Express.* 2011;2(6):1757-1768.
19. Tanna P, Kasilian M, Strauss R, Tee J, Kalitzeos A, Tarima S, Visotcky A, Dubra A, Carroll J, Michaelides M. Reliability and repeatability of cone density measurements in patients with Stargardt disease and RPGR-associated retinopathy. *Invest Ophthalmol Vis Sci.* 2017;58(9):3608-3615.
20. Dubra A, Harvey Z. Registration of 2D images from fast scanning ophthalmic instruments. In: Fischer B, Dawant B and Lorenz C editors. *Registration of 2D images from fast scanning ophthalmic instruments. Biomedical Image Registration*; Berlin: Springer-Verlag; 2010.
21. Salmon AE, Cooper RF, Langlo CS, Baghaie A, Dubra A, Carroll J. An automated reference frame selection (ARFS) algorithm for cone imaging with adaptive optics scanning light ophthalmoscopy. *Transl Vis Sci Technol.* 2017;6(2):9.
22. Chen M, Cooper RF, Han GK, Gee J, Brainard DH, Morgan JI. Multi-modal automatic montaging of adaptive optics retinal images. *Biomed Opt Express.* 2016;7(12):4899-4918.

23. Emsley H. *Visual Optics*. 5 ed. London, UK: Butterworth & Co. Visual Optics.
24. Schneider CA, Rasband WS, Eliceiri KW. NIH Image to ImageJ: 25 years of image analysis. *Nature Methods*. 2012;9(7):671-675.
25. Cunefare D, Cooper RF, Higgins B, Katz DF, Dubra A, Carroll J, Farsiu S. Automatic detection of cone photoreceptors in split detector adaptive optics scanning light ophthalmoscope images. *Biomed Opt Express*. 2016;7(5):2036-2050.
26. Bland JM, Altman DG. Measuring agreement in method comparison studies. *Statistical Methods in Medical Research*. 1999;8(2):135-160.
27. Bartlett JW, Frost C. Reliability, repeatability and reproducibility: Analysis of measurement errors in continuous variables. *Ultrasound Obstet Gynecol*. 2008;31(14):466-475.
28. Zhang T, Godara P, Blancob ER, Griffin RL, Wang X, Curcio CA, Zhang Y. Variability in human cone topography assessed by adaptive optics scanning laser ophthalmoscopy. *Am J Ophthalmol*. 2015;160(2):290-300.
29. Wang Y, Bensaid N, Tiruveedhula P, Ma J, Ravikumar S, Roorda A. Human foveal cone photoreceptor topography and its dependence on eye length. *eLife*. 2019;8:e47148.
30. Wilk MA, Wilk BM, Langlo CS, Cooper RF, Carroll J. Evaluating outer segment length as a surrogate measure of peak foveal cone density. *Vision Res*. 2017;130:57-66.
31. Matet A, Kohl S, Baumann B, Antonio A, Mohand-Said S, Sahel JA, Audo I. Multimodal imaging including semiquantitative short-wavelength and near-infrared autofluorescence in achromatopsia. *Sci Rep*. 2018;8(1):5665.
32. Cava JA, Allphin M, Mastey RR, Cooper RF, Carroll J. Assessing interocular symmetry of foveal cone density. *Invest Ophthalmol Vis Sci*. 2019;60(9):E-Abstract: 4578.
33. Zobor D, Werner A, Stanzial F, Benedicenti F, Rudolph G, Kellner U, Hamel C, Andréasson S, Zobor G, Strasser T et al. The clinical phenotype of *CNGA3*-related achromatopsia: Pretreatment characterization in preparation of a gene replacement therapy trial. *Invest Ophthalmol Vis Sci*. 2017;58(2):821-832.

34. Aboshiha J, Luong V, Cowing J, Dubis AM, Bainbridge JW, Ali RR, Webster AR, Moore AT, Fitzke FW, Michaelides M. Dark-adaptation functions in molecularly confirmed achromatopsia and the implications for assessment in retinal therapy trials. *Invest Ophthalmol Vis Sci*. 2014;55(10):6340-6349.
35. Davidson B, Kalitzeos A, Carroll J, Dubra A, Ourselin S, Michaelides M, Bergeles C. Automatic cone photoreceptor localisation in healthy and Stargardt afflicted retinas using deep learning. *Sci Rep*. 2018;8(1):7911.
36. Cunefare D, Fang L, Cooper RF, Dubra A, Carroll J, Farsiu S. Open source software for automatic detection of cone photoreceptors in adaptive optics ophthalmoscopy using convolutional neural networks. *Sci Rep*. 2017;7(1):6620.
37. Cunefare D, Langlo CS, Patterson EJ, Blau S, Dubra A, Carroll J, Farsiu S. Deep learning based detection of cone photoreceptors with multimodal adaptive optics scanning light ophthalmoscope images of achromatopsia. *Biomed Opt Express*. 2018;9(8):3740-3756.
38. Curcio CA, Sloan KR, Kalina RE, Hendrickson AE. Human photoreceptor topography. *J Comp Neurol*. 1990;292(4):497-523.
39. Baseler HA, Brewer AA, Sharpe LT, Morland AB, Jägle H, Wandell BA. Reorganization of human cortical maps caused by inherited photoreceptor anomalies. *Nat Neurosci*. 2002;5(4):364-370.

**Table 1.** Subject characteristics.

Subject ID	Sex	Age at Imaging (years)	Gene Affected	BCVA, LogMAR OD	BCVA, LogMAR OS
JC_0047*	M	17	<i>CNGB3</i>	0.78	0.90
JC_10024*	M	27	<i>CNGB3</i>	0.92	0.88
JC_10069*	M	22	<i>CNGA3</i>	0.82	0.80
JC_10089*	F	40	<i>CNGB3</i>	1.06	0.86
JC_10151*	F	10	<i>CNGB3</i>	0.98	0.90
JC_10167*	F	16	<i>CNGB3</i>	1.54	1.54
JC_10191*	M	35	<i>CNGB3</i>	0.70	0.68
JC_10195*	M	8	<i>CNGB3</i>	0.82	0.78
JC_10196*	F	33	<i>CNGB3</i>	0.86	0.74
JC_10197*	F	8	<i>CNGB3</i>	0.94	1.02
JC_10198*	F	44	<i>CNGB3</i>	0.96	1.02
JC_10216*	M	17	<i>CNGB3</i>	0.82	0.80
JC_10224*	M	37	<i>CNGB3</i>	0.68	0.72
JC_10232*	M	19	<i>CNGB3</i>	0.76	0.80
JC_10247*	M	24	<i>CNGB3</i>	1.42	1.46
JC_10248*	F	16	<i>CNGB3</i>	0.82	0.82
JC_10310*	M	33	<i>CNGB3</i>	0.78	0.88
JC_10853*	F	28	<i>CNGB3</i>	0.78	0.82
JC_10854*	M	32	<i>CNGB3</i>	0.66	0.76
JC_10999	F	9	<i>CNGB3</i>	0.78	0.64
JC_11062	F	41	<i>CNGA3</i>	0.88	0.88
JC_1208*	M	17	<i>CNGB3</i>	0.86	0.90
MM_0162*	F	17	<i>CNGB3</i>	0.72	0.76
MM_0328	F	23	<i>CNGB3</i>	0.78	0.70
MM_0345	F	32	<i>CNGB3</i>	0.80	0.82
MM_0361	F	26	<i>CNGB3</i>	0.80	0.82

\*Subjects previously reported.<sup>8-17</sup>

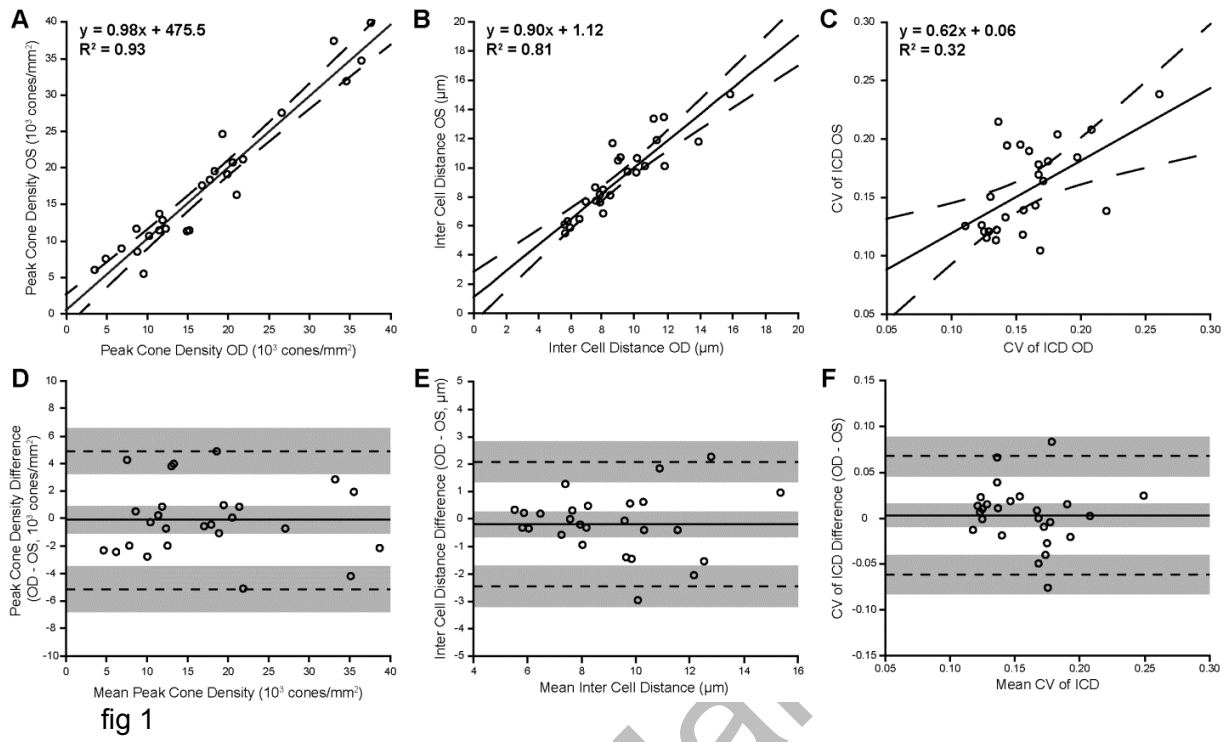
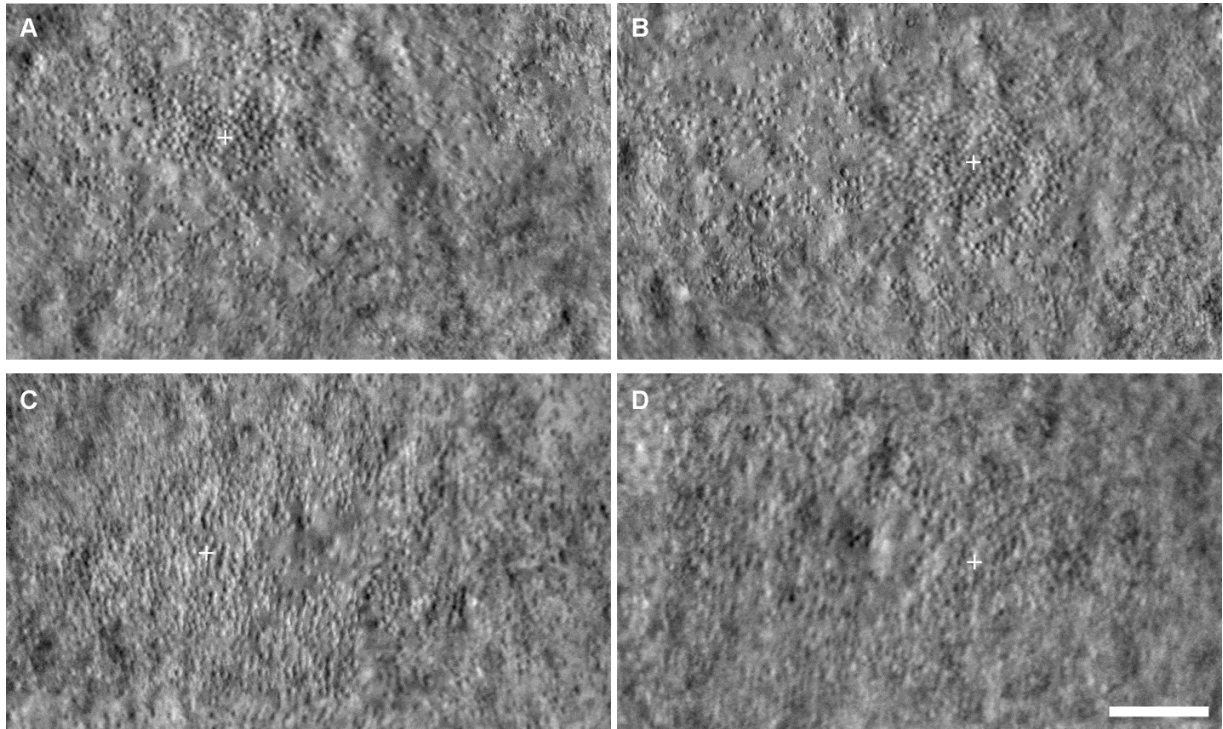


fig 1

Accepted Manuscript

fig 2



Accepted

Fig 3

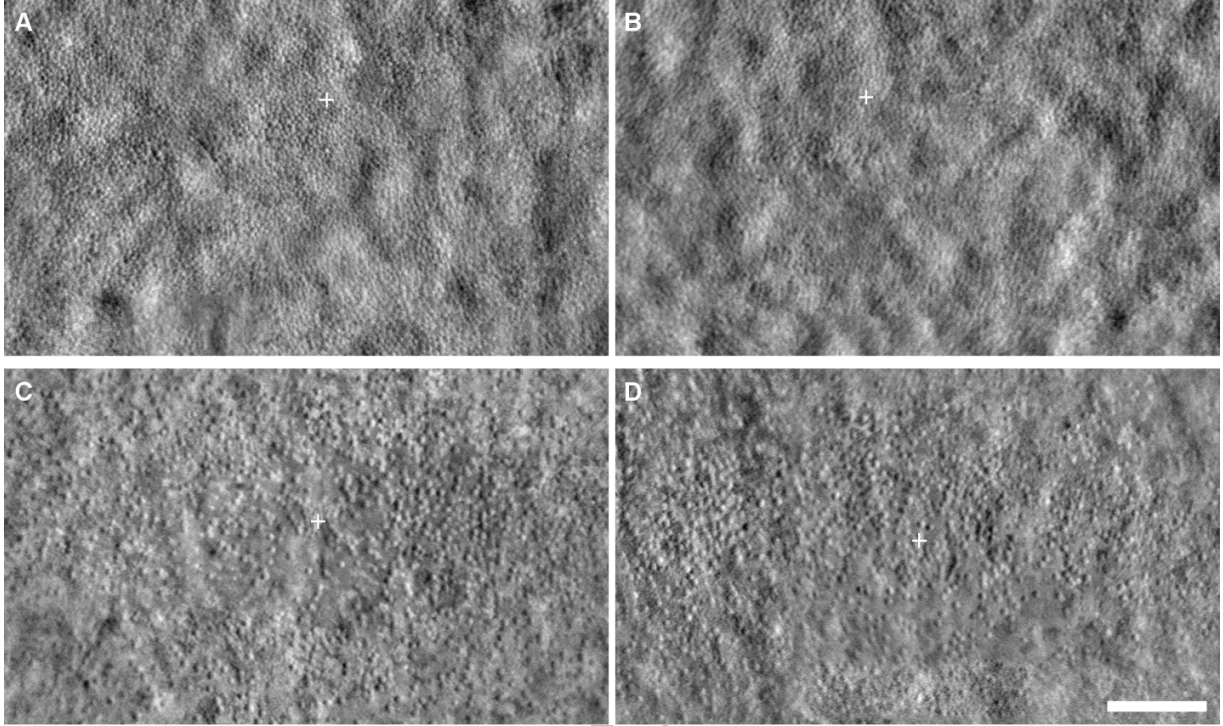
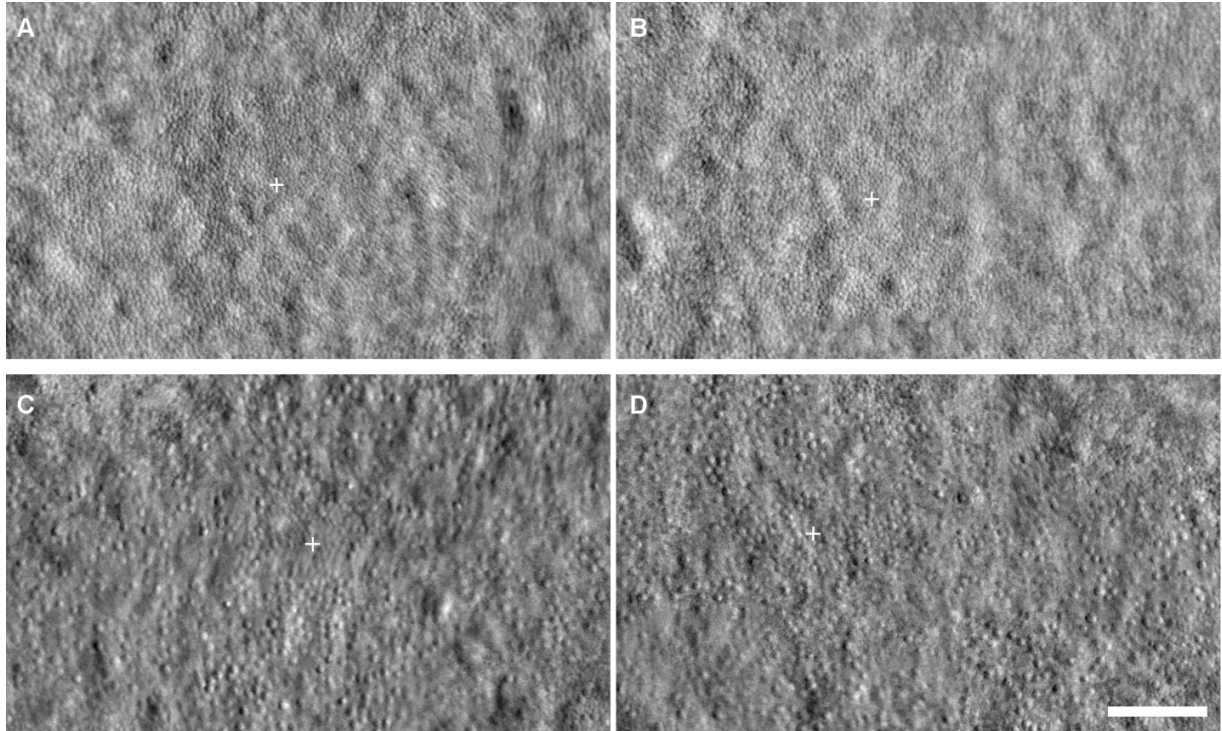
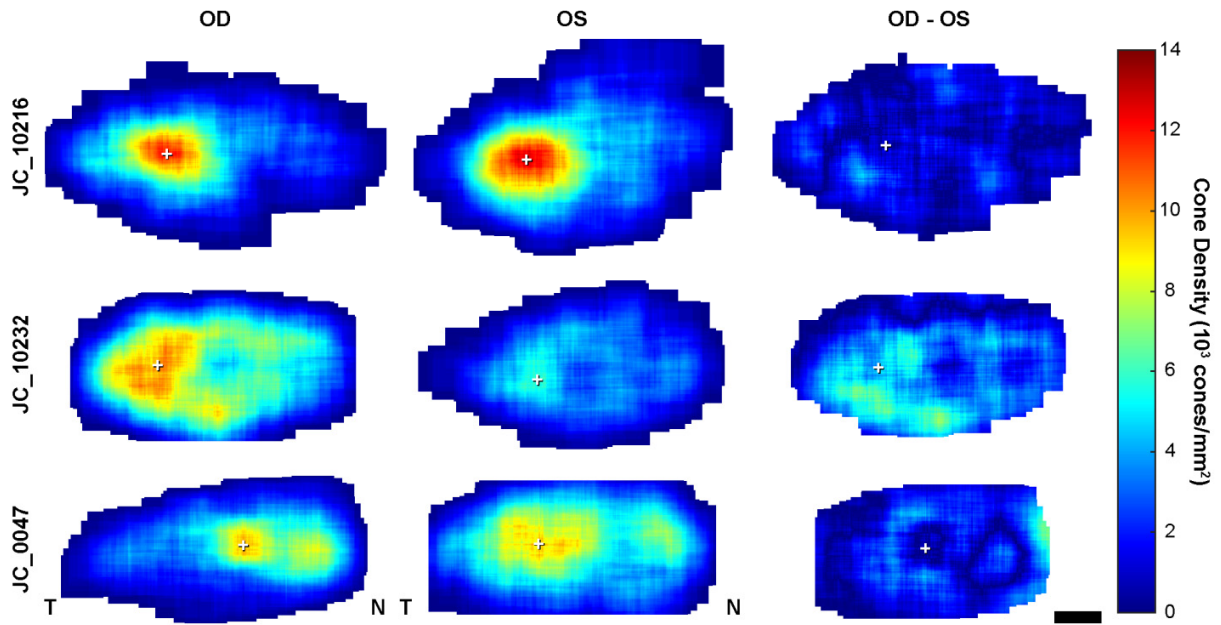


Fig 4



Accepted

fig 5



Accepted Manuscript